Continuous flow aqueous synthesis of highly luminescent AgInS_2 and AgInS_2 /ZnS quantum dots

Céline Rivaux, Tugce Akdas, Ranjana Yadav, Omar El-Dahshan, Davina Moodelly, Wai Li Ling, Dmitry Aldakov, Peter Reiss

Continuous Flow Aqueous Synthesis of Highly Luminescent $AgInS_2$ and $AgInS_2$/ZnS Quantum Dots

Céline Rivaux,[1] Tugce Akdas,[1] Ranjana Yadav,[1] Omar El-Dahshan,[1] Davina Moodelly,[1] Wai Li Ling,[2] Dmitry Aldakov,[1] Peter Reiss[1,*]

[1] Univ. Grenoble Alpes, CEA, CNRS, IRIG, SyMMES, STEP, 38000 Grenoble, France

[2] Univ. Grenoble Alpes, CEA, CNRS, IBS, 38000 Grenoble, France

*Corresponding author email: peter.reiss@cea.fr

Abstract

Continuous flow synthesis of semiconductor quantum dots (QDs) holds the promise of being highly reproducible, scalable, and providing precise control of all reaction parameters. Here, we applied this technique to the aqueous synthesis of Ag-In-S (AIS) core and AIS/ZnS core/shell QDs and optimized several parameters comprising reaction temperature, pressure, time, nature, and the ratio of precursors. Photoluminescence quantum yield (PLQY) values of 32%/44% (average/best) for the core and 77%/83% for the core/shell system have been obtained in short reaction times (8-15 min). We demonstrate by means of combined structural and optical studies that the high PLQY originates from donor-acceptor pair recombination processes, involving essentially [In_{Ag}^{2+} + 2 V_{Ag}^{-}] defect complexes whose formation is favored by the large excess of indium used (In:Ag ratio of 4:1), and the low reaction temperature (100-120°C). The structural disorder is further enhanced during ZnS shell growth, which in addition to surface passivation and removal of non-radiative decay channels, leads to the partial diffusion of the added zinc ions into the AIS core and the formation of Zn_{In} antisite defects. The presented

method provides excellent reproducibility and high scalability, facilitating the large-scale production of highly luminescent AIS/ZnS QDs.

Introduction

Colloidal quantum dots (QDs) have attracted a lot of attention in the past four decades because of their unique size-dependent electronic and optical properties. Most research has focused on QDs with binary compositions, i.e., composed of II-VI, III-V, and IV-VI semiconductors, such as CdSe, CdTe, and PbS due to their size-tunable light emission, broad absorption spectrum enabling the excitation of multiple fluorescence colors with a single source, high brightness, and long-term photostability.[1-5] These outstanding properties make them ideal candidates for a wide range of applications, including biosensing,[6] drug delivery,[7] bioimaging,[8] LEDs,[9] and photocatalysis.[10] However, the toxicity of these QDs due to the presence of Cd or Pb limits their potential for real-life applications, especially in the biomedical field.[11] Therefore, currently large efforts focus on the development of safer and more environmentally friendly QDs.[12-14] This evolution has led to a growing interest in ternary I-III-VI_2 chalcopyrite QDs (I: Cu, Ag; III: In, Al, Ga, Bi; VI: S, Se, Te), with the most widely studied examples being $CuInS_2$ (CIS)[15-18] and $AgInS_2$ (AIS).[19, 20] In contrast to traditional binary QDs, ternary QDs exhibit a much larger Stokes shift and photoluminescence (PL) linewidth (both typically on the order of some hundreds of meV), long PL lifetimes (hundreds of nanoseconds), and strong composition dependence of their optical and electronic properties.[21, 22, 23]

The colloidal synthesis of ternary I-III-VI QDs, often adapted from binary II-VI nanocrystal syntheses, is more difficult to set up because it is necessary to control the relative reactivity of the two different metal cation precursors with the sulfur precursor in the reaction medium. They are mostly performed in organic solvents, and therefore, the obtained QDs cannot be directly applied in biological studies or in photocatalytic reactions taking place in

water. The phase transfer from organic to aqueous medium implies additional steps and is generally associated with a significant decrease in the PL quantum yield (PLQY) and colloidal stability. As an appealing alternative, the direct synthesis in the aqueous phase has been developed.[24] While the reaction conditions are in most cases much less stringent than in the organic synthesis of QDs, the reaction mechanism is more difficult to elucidate due to the complex interplay of multiple parameters. In particular, the complexation of metal ions in presence of organic ligands, the reactivity of the formed complexes as well as that of the chalcogenide source are generally strongly dependent on the pH value of the reaction medium, which itself depends on the species generated during the chemical transformations. The pH also governs the formation of metal hydroxides, which can occur either in the solubilized or the solid state.[24] In 2017, Raevskaya et al. synthesized mercaptoacetic acid (MAA) stabilized AIS QDs using a simple heat-up approach.[25] AIS/ZnS core/shell QDs obtained after passivation with Zn^{2+} ions exhibited a high PLQY in the range of 40-50%. However, the drawback of this synthesis is the polydispersity of the obtained QDs. The same group optimized the synthetic protocol by replacing MAA with glutathione (GSH) in the presence of citric acid and using a precursor ratio of Ag:In:S = 1:4:5.[26] The core and core/shell QDs exhibited a PLQY of 32% and 60%, respectively. Martynenko et al. recently adapted this synthesis using microwave heating to prepare mercaptopropionic acid (MPA) stabilized AIS core and AIS/ZnS core/shell QDs, which allowed reducing the reaction time to 5 min and achieving a PLQY of 66% with the core/shell QDs emitting at 638 nm.[27]

Despite these optimizations, several intrinsic problems cannot be solved by conventional batch synthesis techniques. In particular, the quality of the QDs in terms of emission peak position, linewidth, and PLQY can vary from batch to batch due to subtle changes in the experimental parameters, making it difficult to ensure consistency and reproducibility between several experiments. Continuous flow chemistry has recently emerged

as a promising approach for the synthesis of high-quality colloidal QDs.[28] It offers the potential to produce QDs with tighter size control and higher reproducibility by precisely adjusting the reaction conditions (e.g., heating/cooling rates, reaction time) due to improved heat and mass transfer in small tubular reactors.[29] It also gives access to faster and automated reactions and allows for rapid reaction optimization while enabling reaction conditions that are not achievable with standard batch methods, such as the homogeneous rapid heating of the entire reaction volume eventually combined with increased pressure. In spite of these advantages, the flow chemistry approach has not yet been widely explored for AIS QDs and previous research focused mainly on binary QDs or more recently on lead halide perovskite nanocrystals.[30] In one example, Li et al. developed the flow synthesis for composition-tunable AIZS/ZnS and CIZS/ZnS QDs in organic media (Z stands for Zn-doped).[31] By modifying the precursor ratio, the emission of these QDs could be varied from 432 to 615 nm and the maximum PLQY of CIZS/ZnS reached 40%. In 2019 Ma et al. synthetized $AgInS_2$ (capped with MPA) in droplet microreactors, achieving a PLQY of 8.8% with a maximum PL wavelength of 725 nm.[32] Here, we present a rapid two-step method using flow chemistry for the preparation of GSH-capped AIS/ZnS core/shell QDs in the aqueous medium. The obtained QDs exhibit a PLQY up to 83%, which ranges among the highest values obtained with this material so far. The underlying emission mechanism is discussed on the basis of XPS studies and elemental analysis.

Methods

Chemicals

All chemicals were used as received without further purification. L-glutathione reduced (GSH, ≥ 98 %), indium chloride ($InCl_3$, 99.999 % trace metal basis), ammonium hydroxide (NH_4OH, ACS reagent, 28.0-30.0 % NH_3 basis), ammonium sulfide ($(NH_4)_2S$, 40-48%wt solution in water) and zinc acetate dihydrate ($Zn(OAc)_2{\cdot}2H_2O$, ≥ 97 %) were purchased from Sigma-

Aldrich. Sodium sulfide nonahydrate ($Na_2S{\cdot}9H_2O$, ACS, ≥ 98.0 %) was purchased from Alfa Aesar. Nitric acid (65 %), Propan-2-ol (HPLC isocratic grade) were purchased from Carlo Erba. Silver nitrate (99.995%), citric acid (anhydrous, 99.5 %), and rhodamine 6G (99%) were purchased from Arcos Organics. Thiourea (99 %) was purchased from VWR. Milli-Q ultrapure water (18.2 MΩ.cm) was used in all experimental procedures and analyses.

Preparation of the stock solutions

Stock solution of the GSH/In/Ag mixture:

In a typical procedure, 1.2 mmol of GSH was solubilized in 1.9 mL of water and 0.5 mL of 0.25 M NH_4OH by using an ultrasound bath for 5 minutes. 0.8 mmol of $InCl_3$ was dissolved in 0.9 mL 0.25 M HNO_3 and finally both solutions were mixed with 2 mL of water. The pH of the obtained mixture was raised from 3.5 to 9 by adding 1.3 mL of 5.0 M NH_4OH under intense stirring. The addition of ammonia induced the formation of a white precipitate, which dissolved after 2−3 min of vigorous mixing. Next, 0.2 mmol of $AgNO_3$ diluted in 2.0 mL Milli-Q water was introduced, and finally, some drops of a 2.0 M aqueous solution of citric acid were added to adjust the pH close to 7.

Stock solution of the sulfur precursor:

A solution of 1 mmol of Na_2S or $(NH_4)_2S$ in 8 mL of water is prepared directly before the synthesis.

Stock solution for ZnS shell growth:

1.2 mmol of GSH, 0.8mmol, $Zn(Ac)_2$ and 0.8 mmol of thiourea are mixed with 10 mL of water. The pH is adjusted at 7 with 5N NH_4OH.

Continuous flow synthesis of AIS and AIS/ZnS QDs

Milli-Q water is the solvent for all syntheses, performed using the Asia flow chemistry system by Syrris® configured with pump syringes, automatic reagent injector, heater, backpressure controller, and sample collector. The two sample loops had a volume of 5 mL, which limited the volume of the resulting QD colloidal solution to around 9 mL. The heater used was a 4 mL stainless steel tubular reactor with an inner tube diameter of 1 mm (see sup. info for picture and scheme). A Tee section was placed after the injectors and before the heater to enable the mixing of the metal and sulfur precursor solutions at room temperature, just before arriving at the heating stage. The system was used in the automatic mode, which means that the flow rate was automatically calculated according to the desired residence time (reaction time).

For the AIS core QD synthesis, equal volumes of the GSH/In/Ag stock solution and the sulfur precursor solution were placed in two automatic reagent injectors and different parameters were explored: temperature (80°C, 100°C, 120°C, and 150°C), pressure (3, 5 et 8 bar), residence time (8, 10, 15 and 30 min). An alternative precursor of sulfur $(NH_4)_2S$ was also tested. For the AIS/ZnS core/shell QD synthesis, the AIS core QDs and the shell precursor stock solutions were in the reagent injectors and the following parameters were explored: temperature (100°C and 120°C), pressure (3 and 5 bar) and residence time (8, 10 and 15 min).

Both AIS and AIS/ZnS QDs were purified by adding one volume equivalent of 2-propanol. This addition results in the precipitation of the QDs, and the precipitate can be separated by centrifugation (10 min at 10 000 rpm) and redissolved in the desired volume of deionized water.

Characterization

For all optical spectroscopy, the aqueous colloidal solutions were placed in 4x10 mm quartz cuvettes. Absorption spectra were recorded using a Hewlett Packard 8452A diode array UV-vis spectrophotometer with a range of 190 to 820 nm. PL spectra were recorded using a Hitachi F-4500 fluorescence spectrophotometer equipped with a 150 W Xe lamp and an R3788

photomultiplier tube detector. An excitation wavelength of 400 nm was used if not stated otherwise and the emission spectrum was recorded at wavelengths from 430 nm to 850 nm at a scan rate of 1200 nm/s. For the comparison of the PL intensity, the spectra were normalized taking into account differences in absorbance at the excitation wavelength.

The optical bandgap (Eg) was determined from the Tauc plots of $(\alpha h\nu)^2$ versus $h\nu$, where α is the absorption coefficient, h is Planck's constant, and ν is the light frequency. The valence band positions were determined using Riken AC-2 Photoelectron Spectrometer (Riken Instruments). PL decay curves were recorded using the time-correlated single-photon counting technique on a Fluorolog-3 spectrometer (HORIBA Jobin Yvon) and a pulsed LED with an excitation wavelength of 352 nm (NanoLED-350, <1 ns pulse, HORIBA) as the excitation source. The curves were fitted with DAS6 analysis software provided by HORIBA Scientific.

The luminescence lifetime reflects the possible recombination paths involved in the emission of the QDs. The resulting decay signal can be simulated by a sum of exponential functions, each corresponding to a distinct recombination path. The accuracy of this exponential fit is given by the $\chi 2$ factor, which should be as small as possible ($\chi 2$ close to 1). As in the overwhelming majority of literature examples analyzing the TRPL behavior of ternary chalcopyrite type QDs,[19] fitting of the decay curves required a triple exponential model, in particular, to achieve an accurate fit in the short time region:

$$I(t) = A_1\, e^{(-t/\tau_1)} + A_2\, e^{(-t/\tau_2)} + A_3\, e^{(-t/\tau_3)} \quad ,$$

where τ is the decay time and A is the relative amplitude of each decay component.

The PL quantum yield (PLQY) was determined using an integration sphere mounted on the Fluorolog spectrometer. Furthermore, control measurements were made relative to rhodamine 6G (QY in ethanol: 95%). The absorbance of the rhodamine 6G and the QDs samples at the excitation wavelength were made identical (0.04, 0.06, 0.08, or 0.10) by adjusting their concentrations. Plotting the area of the integrated fluorescence intensity versus absorbance

resulted in straight lines whose slopes were used to calculate the PLQY of the QDs according to:

$QY_{QD} = QY_{rhodamine6G} * (slope_{QD}/slope_{rhodamine\ 6G}) * (\eta_{water}/\eta_{EtOH})^2 \times 100$

with η being the refractive index.

Morphological characterization was achieved via TEM analysis, using a Tecnai F20 Microscope and an accelerating voltage of 200 kV. A drop of the dilute QD dispersion was placed on an amorphous carbon substrate on a copper grid and dried in air. The average diameter and size distribution of the core and core-shell QDs were calculated based on the measurement of at least 100 nanoparticles selected by eye and using ImageJ processing software. The standard error (*S.E.*) in the values was calculated using the following equation:

$S.E. = \sigma\sqrt{n}$

where σ is the standard deviation of the sample and n is the number of measurements taken.

The XRD diffraction patterns were recorded using a Philips X'Pert diffractometer with Cu Kα radiation, λ = 1.5406 Å, from 2θ = 10 to 80°.

X-ray photoelectron spectroscopy (XPS) analyses were carried out with a Versa Probe II spectrometer (ULVAC-PHI) equipped with a monochromated AlKα source (hν = 1486.6 eV). The core-level peaks were recorded with a constant pass energy of 23.3 eV. The XPS spectra were fitted with CasaXPS 2.3 software using Shirley background. Binding energies are referenced with respect to adventitious carbon (C 1s BE = 284.8 eV).

ICP-AES measurements were performed on a Shimadzu 9000 spectrometer. The samples were prepared by adding 10 µL aqueous colloidal solution of each synthesis in 6 mL with 10% HNO_3. Standards solutions of the metal ions were prepared by diluting ICP standards of Ag, In, and Zn with HNO_3 10% (v/v). Subsequently, calibration curves were established for the concentration range relevant to our samples. Ag was detected at a wavelength of 338.289 nm, In at 325.609 nm, and Zn at 213.856, respectively.

Proton NMR spectra were recorded on a Bruker Avance™III HD NanoBay NMR spectrometer (400 MHz) and analyzed using TopSpin 3.6.2 software. For the sample preparation, 3-4 mg of purified and dried QDs were diluted in 500 µl of D_2O. Analyses of the Zeta potential and Dynamic light scattering (DLS) were carried out at 25 ± 2 °C using a Litesizer 500 (Anton Paar, 40 mW semiconductor diode laser light, wavelength λ = 658 nm).

Results & Discussion

In the case of ternary QDs, the reactivity of the two metal cation precursors has to be balanced by means of complexation with appropriate ligands. The most commonly used metal precursors in the aqueous batch-type synthesis of AIS QDs are silver nitrate and indium nitrate or chloride. These compounds are highly reactive with sulfur, and therefore, carboxylates (e.g., citric acid or sodium citrate) are added to the reaction medium to control the reactivity of the indium precursor, while thiol ligands (e.g., GSH, D-penicillamine, MAA, MPA) are applied to mediate the reactivity of the silver precursor. The pH of the reaction medium is generally set above 8 to deprotonate the ligands and assure the solubility of the metal complex intermediates. Na_2S is the most widely used sulfur precursor despite its high reactivity and toxicity. For the development of the continuous flow synthesis of AIS core QDs, we took the batch synthesis reported by Stroyuk and coworkers as a starting point, applying in all experiments an In:Ag ratio of 4:1.[26] This reaction scheme is fully compatible with the requirements of flow chemistry in terms of precursor solubility and absence of volatile reaction products. In contrast to typical batch syntheses, the flow setup enables the fast and precise screening of reaction parameters including hydrothermal conditions, i.e., temperatures >100°C and increased pressure. In the present case, two channels are used, one for the mixed metal precursor solution, and the other for the sulfur precursor solution (cf. **Fig. S1**, Supp. Inf.). Comparative experiments revealed that mixing both channels at room temperature in a Tee connector just before entering the

heating stage (mimicking a heat-up synthesis) worked better than mixing them within the heater (similar to a hot-injection synthesis). In the latter case, a small fraction of larger-sized black particles formed, which led to the clogging of the tubes after a few experiments. For the core/shell synthesis, the same strategy was applied, premixing the AIS core nanoparticles and the ZnS precursor solution in the Tee connector before entering the heating stage.

Figure 1a shows the XRD patterns of the $AgInS_2$ and $AgInS_2$/ZnS QDs obtained using optimized conditions (100°C / 3 bar) as well as a residence time of 8 min (core) and 15 min (core/shell). The resulting diffractogram of the core is characterized by three broad signals centered at 27.1°, 45.0°, and 53.0°, which are attributed to the (112), (204), and (312) peaks of the tetragonal chalcopyrite phase of AIS (JCPDS 00-025-1330). Nonetheless, due to a significant linewidth of the peaks, the presence of other phases, like cubic $AgIn_5S_8$ (JCPDS No. 25-1329) or orthorhombic $AgInS_2$ (JCPDS No. 25-1328), cannot be fully excluded. Compared to the core, the peaks of the core/shell sample are slightly shifted to higher angles, toward the characteristic positions of zinc blende ZnS (JCPDS 01-071-5975). This shift has been widely reported in AIS/ZnS studies and indicates the successful growth of ZnS around the inorganic QD core.[33-35] Given the smaller lattice parameter of ZnS, the origin of this shift can be explained by the compressive strain exerted by the ZnS shell. On the other hand, cation exchange and zinc diffusion into the AIS nanocrystals may also occur and contribute to the lattice contraction. To determine the role of cation exchange, the change of the In:Ag ratio after the addition of ZnS was monitored using ICP-OES (cf. **Table S1**, Sup. Inf.). We observed in all syntheses that the In:Ag ratio measured for the core AIS nanocrystals decreased during the shell growth. This behavior confirms that cation exchange indeed occurs and that preferentially indium atoms are replaced by zinc atoms during the ZnS shell growth.

As generally observed for I-III-VI ternary compounds, the UV-vis absorption spectra of the AIS core and AIS/ZnS core/shell QDs do not exhibit distinct excitonic features.[25, 26, 34] In

addition to the size distribution, inhomogeneities in the composition of the nanocrystals as well as particle-to-particle variations in the nature and density of defect states contribute to the spectral broadening. The core/shell sample exhibits a stronger absorbance in the UV range, which is attributed to the contribution of the ZnS shell. Shell growth is in all cases accompanied by a widening of the band gap as determined from Tauc plots using the UV-vis absorption data (cf. **Fig. S2**). This behavior, attributed to the aforementioned Zn diffusion into the AIS core, contrasts with that observed in binary core/shell QDs (e.g., InP/ZnS, CdSe/ZnS) where shell growth induces a red-shift of the absorption and emission spectra due to the leakage of the electron/hole wave function into the shell.[36] The actual band gap difference between the core (around 2.5-2.8 eV) and core/shell (around 2.6-3.1 eV) QDs depends on the synthetic conditions of both and varies in the present study from 50 to 580 meV. In all cases, the values are remarkably higher than the band gap energy of bulk chalcopyrite $AgInS_2$ (1.87 eV), which can be related to the off-stoichiometry due to the Ag-poor conditions used and to quantum confinement effects, as the particle size is much smaller than the Bohr exciton radius of 5.5 nm (vide infra). Both the core and core/shell QDs exhibit significant absorption below the band gap energy (the so-called Urbach tail) related to disorder.[37] To measure the absolute positions of the energy bands, we have used photoelectron spectroscopy in air (PESA) of the QD films. The analysis showed that the position of the valence band (-5.60 eV) does not change for the core and core/shell QDs, which is expected taking into account that in AIS and AIS/ZnS QDs it is composed of S 3p and Ag 4d hybrid orbitals.[38] Considering the band gap of 2.58 eV for the core and 2.63 eV for the core/shell QDs (sample presented in **Fig. 1**), the conduction band levels can thus be calculated as -3.02 and -2.97 eV, respectively.

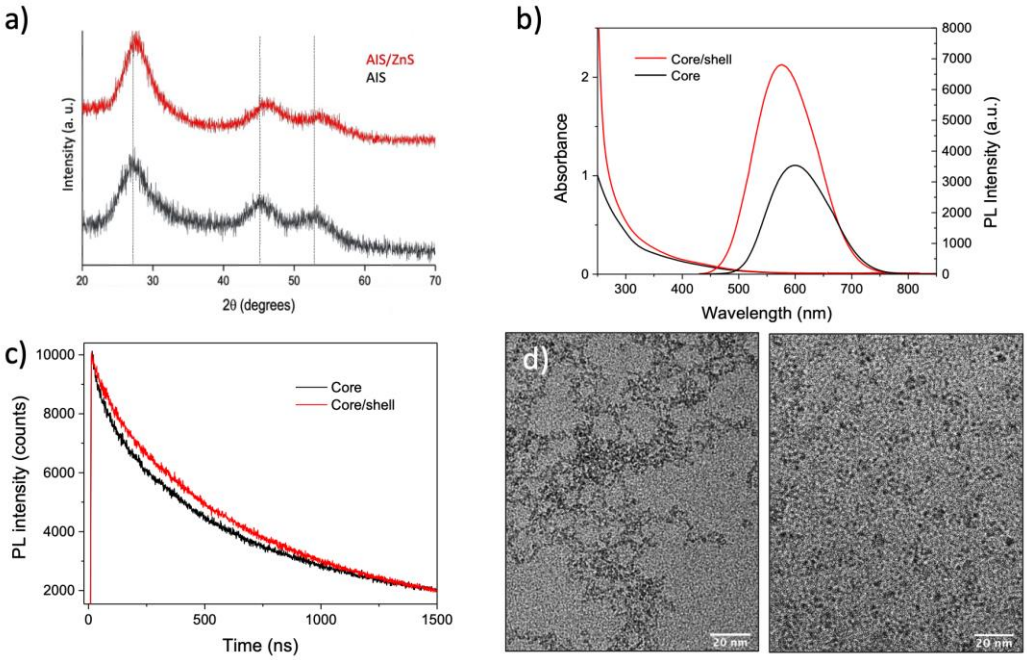

Figure 1: Comparison of the obtained AIS core and AIS/ZnS core/shell nanocrystals. a) X-ray diffraction patterns; b) UV-vis and steady-state PL spectra; c) TRPL decay curves; d) TEM images (left: AIS, particle size 1.67 ± 0.6 nm; right: AIS/ZnS, 2.35 ± 0.8 nm).

The emission from Ag-In-S nanocrystals has been attributed to be dominated by radiative recombination related to intrinsic donor-acceptor defects as well as surface-related defects due to the high surface-to-volume ratio of the QDs.[21, 39, 40] The PL spectrum of the AIS core QDs (**Fig. 1b**) shows a broad peak centered at 610 nm with a linewidth (FWHM) of around 120 nm (400 meV) and redshifted from the band gap energy by 570 meV. These large values are typical for emission processes involving mid-gap states.[21,37] The PLQY of the AIS core QDs ranged between 28% and 44% (average 32%) depending on the experimental conditions (vide infra) and was 38% for the sample shown here. In the broader context of diverse types of colloidal semiconductor QDs, these values are very high for as-synthesized core QDs. Moreover, it has to be underlined that the AIS QDs are prepared in environmentally benign conditions in the aqueous phase at temperatures around 100°C. The PL spectrum of the

AIS/ZnS core-shell QDs shows two significant differences from the core sample: first, the emission wavelength is blue-shifted by 30 nm relative to the core emission wavelength of 610 nm. This hypsochromic shift is a common feature in CIS and AIS QDs after passivation with a ZnS shell and is explained as above by Zn diffusion into the AIS core and the associated widening of the band gap. Second, compared to the core, a significant increase in the emission intensity was observed leading to PLQYs in a range of 63-83% with an average of 77% (80% for the sample in **Fig. 1b**). This increase is associated with the passivation of surface traps eliminating non-radiative recombination pathways of the photogenerated electron-hole pairs. Time-resolved PL (TRPL) measurements are an appropriate tool for investigating the underlying recombination channels. In the analysis of the TRPL data (**Fig. 1c**), two exponentials were not sufficient to simulate the experimental curves. In particular, to assess the short lifetime component correctly, it is necessary to add a third function despite its small contribution (1% or less, cf. **Table 1**).

Table 1: PL lifetime analysis of the AIS core and AIS/ZnS core/shell QDs presented in **Fig. 1**.

Sample	$\tau 1$ (ns) - A_1	$\tau 2$ (ns) - A2	$\tau 3$ (ns) - A3	X^2	$\tau_{average}$ (ns)
AIS core	22 - 1%	217 - 30%	1006 - 69%	1.16	938
AIS/ZnS core/shell	22 - 0.4%	250 - 27%	1344 - 73%	1.18	1273

In AIS-related QDs, the short lifetime component ($\tau 1$) on the order of 20-50 ns has been attributed to the intrinsic radiative recombination of surface states, while the medium ($\tau 2$) and long ($\tau 3$) lifetimes on the order of several hundred nanoseconds have been proposed to arise from donor-acceptor pair (DAP) recombination involving surface states and core states of the QDs, respectively.[19, 41, 42] As expected, the passivation of the AIS QDs with a ZnS shell decreases the density of surface-related defects and hence the contribution of $\tau 1$. Furthermore, $\tau 2$ increases by ~30 ns and shows a decreased contribution in AIS/ZnS, which indicates the

filling of defect sites closer to the surface (e.g., Ag or In vacancies) by diffusing Zn^{2+} ions. All in all, the combination of these effects leads to an increase in the average PL lifetime from 938 to 1273 ns, which is indicative of a lower contribution of non-radiative recombination enhancing the PLQY.

Transmission electron microscopy (TEM) analysis (**Fig. 1d**) turned out challenging due to the small diameters of the AIS core (1.67± 0.6 nm) and AIS/ZnS core/shell (2.35± 0.8 nm) QDs and the related low contrast; the size histograms are given in **Fig. S3** (Supp. Inf.). The observed mean size increase of 0.68 nm corresponds to a ZnS shell thickness of around 1.1 monolayers. These small particle sizes are also close to the lower limit commonly accessible with dynamic light scattering (DLS) techniques, which give access to the hydrodynamic diameter. Our measurements on a large number of samples yielded a mean value of 3.80±0.5 nm and 13.5±2.9 nm for the AIS core and AIS/ZnS core/shell QDs, respectively, with a polydispersity index (PDI) of ca. 0.2 (cf. **Fig. S4**). The significantly higher values than those determined by TEM arise from the hydration corona at the periphery of the particles. Moreover, the thickness of this hydration sphere appears to be much larger in the case of the core/shell nanocrystals, which has been consistently observed for all samples studied. The surface charge is a key parameter that affects the colloidal stability of the QDs. It was determined by zeta potential (ξ) measurements (**Fig. S4**) resulting in an average value of -25 mV for the AIS core and -30 mV for the AIS/ZnS core/shell nanocrystals. The predominance of a negatively charged surface is due to the deprotonated carboxyl groups ($R\text{-}COO^-$) of the GSH ligands in a neutral or basic medium. The surface state of the QDs was further studied by comparing their proton NMR spectra with that of free GSH. As shown in **Fig. S5**, in addition to a few chemical shift changes for some protons and the characteristic broadening due to the restricted motion of the ligands bound to the QD surface, protons attached to C5 of GSH (adjacent to the thiolate group) on the AIS core showed multiple splitting peaks in the range of 2.9-3.3 ppm. Similar behavior

was observed in the studies of Ag nanoclusters capped with GSH ligands where these changes were attributed to the chirality of the ligands at the nanoparticle surface.[43] Hence, the splitting of the protons bound to C5 is expected to originate from the induction of the chiral carbon C4 and the rotation restriction of the C-S bond after the attachment of GSH to the QD surface. In the case of the core/shell QDs, this splitting is not observed; we note instead a slight splitting of the protons at C2 at around 2.1 ppm. Zn ions at the ZnS surface have a higher affinity for amines than for thiols,[44] while in the case of Ag at the AIS surface the situation is reversed.[45] On the other hand, considering the high In:Ag ratio, AIS core nanocrystals are expected to be mainly In-terminated, which would favor coordination by the carboxylate groups of GSH. Considering these different nanocrystal surface – ligand affinities for the core and core/shell QDs, the observed NMR spectral changes are likely indicative of different surface coordination of the GSH ligands. For both types of QDs, we further note multiple overlapping peaks in the chemical shift range of 3.6–3.8 ppm, attributed to the interactions of the C6 protons with adjacent -NH and -COOH groups once the GSH ligands are bound to the nanocrystal surface (cf. **Fig. S6**). Finally, the presence of a doublet around 2.6 ppm in the spectrum of the AIS core QDs is characteristic for citric acid, which can play the role of a surface ligand in addition to its action of mediating the indium reactivity.

To get further insight into the chemical state of the elements and the composition of the QDs, XPS measurements were performed yielding an Ag:In:S atomic ratio of the AIS core QDs of 1: 3.0 : 6.7, which is in line with ICP-OES results (**Table S1**). High-resolution spectra were recorded for all the key elements (**Fig. 2**; survey spectra cf. **Fig. S7**). The Ag 3d and In 3d spectra show a doublet of the characteristic $3d_{5/2}$ and $3d_{3/2}$ electrons corresponding in energy to Ag^{+} and In^{3+}, respectively, in agreement with previous studies.[26, 46] Surprisingly, in the literature these peaks of AIS are rarely fitted although they can afford very useful information about the structure of this material. In our case, both the Ag and In $3d_{5/2}$ signals can be fitted with two

peaks, at 367.5 and 368.0 eV for Ag, and 444.6 and 445.0 eV for In, respectively. Several explanations can be used to interpret these peaks, such as the presence of partially oxidized elements or the difference in the chemical environment between the surface and core atoms. As the size of our QDs is comparably small, more than 40% of the atoms are located on the surface. On the other hand, we have to consider that the composition of the AIS QDs used in this work is strongly off-stoichiometric, leading to the presence of a high concentration of defects in the lattice. With a large excess of In (In:Ag ratio around 4:1), the principal defects expected are Ag vacancies V_{Ag}^{-} and antisite defects In_{Ag}^{2+} via the formation of [In_{Ag}^{2+}+ 2 V_{Ag}^{-}] defect complexes.[19, 47] The formation of these defects leads to a decrease of electron density at the In atom and its increase at the neighboring Ag atoms, following the trend of their relative electronegativity values. While for most of the elements (including In) electron-poor environments lead to the shift of the XPS signal to higher binding energies, in the case of silver this trend is reversed and the signal of more oxidized Ag appears at lower energies.[48] Accordingly, we can tentatively assign the two deconvoluted peaks of the Ag spectrum as follows: the peak at higher energy (368.0 eV, 86%) is ascribed to Ag atoms close to an antisite defect, while that at 367.5 eV (14%) corresponds to Ag atoms in the regular coordination, not affected by the defect sites. Likewise, in the case of the In $3d_{5/2}$ spectra, the peak at 445.0 eV (89%) is supposed to originate from In atoms on defect sites, while that at 444.6 eV (11%) is assigned to In atoms in the regular AIS environment. We note that a similar interpretation has been reported for ZAIS (AIS/ZnS alloyed) QDs prepared in an organic medium.[49] A strong argument in favor of our hypothesis is the fact that the fraction of the higher energy signal arising from In antisite and Ag vacancy states is approximately the same.

The sulfur signal can be fitted with three doublets of $2p_{3/2}$ and $2p_{1/2}$ species. The $2p_{3/2}$ peak at lower energy (161.5 eV, 59%) corresponds well to the S^{2-} signal arising from the inorganic AIS core while that at 162.7 eV (24%) originates from the thiolate function of the

GSH ligand.[26] Finally, a peak of lower intensity at 168.2 eV (17%) indicates the presence of oxidized species, most likely sulfonates, on the QD surface.

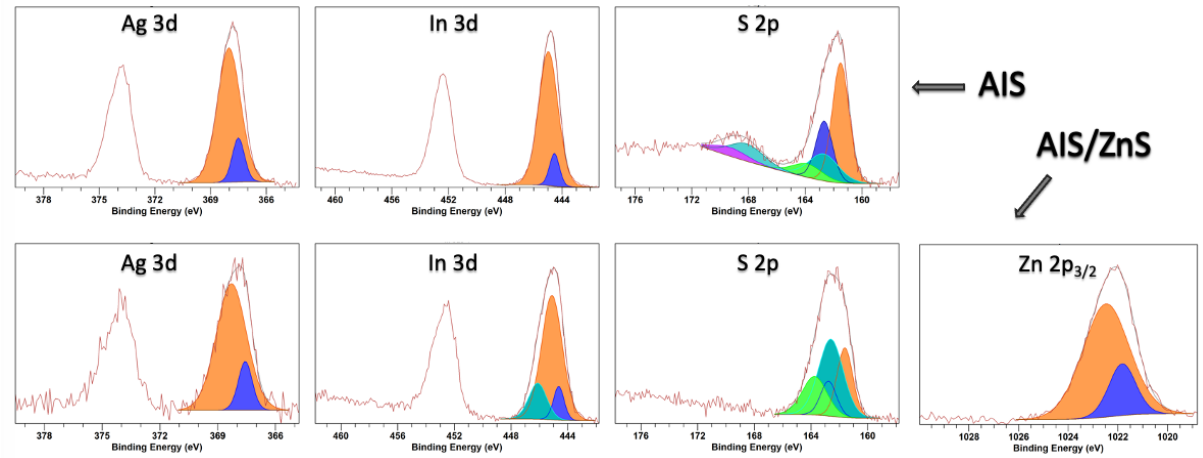

Figure 2: High-resolution XPS spectra of the different elements in the AIS core (top row) and AIS/ZnS core/shell (bottom row) QDs.

For the AIS/ZnS core/shell QDs, the presence of all 4 elements is confirmed (**Fig. 2**, bottom row). The high-resolution signal of Ag is similar to the one observed for AIS with two peaks at 367.6 (15%) and 369.3 eV (85%) assigned once again to the atoms in standard coordination and those close to defects sites, respectively. The slight shift to higher energy with respect to the peaks of AIS is likely due to the energy loss of the electrons of core elements when passing through the ZnS shell. The In signal deconvolution features the appearance of a third peak at higher energy (446.1 eV, 18%) in addition to those already observed for AIS QDs at 444.6 (10%) and 445.1 eV (72%) with a very similar FWHM. To understand the origin of this additional peak, we first referred to the literature, which shows that compounds displaying a signal around 446.1 eV are usually In halogenides, which can be ruled out in our case.[50] As mentioned above, upon introduction of Zn^{2+} to the AIS core, in addition to the ZnS shell formation partial cation exchange is possible, associated with the formation of new types of

defects such as Zn_{In}^{-} (and to a lesser extent Zn_{Ag}^{+})[49] leading to a two-peak Zn $2p_{3/2}$ fitting model corresponding to Zn atoms at AIZS defect sites (peak at 1022.5 eV) and in classical ZnS coordination (1021.8 eV). Consequently, this situation leads to the occurrence of the 3rd In peak corresponding to partially oxidized In in close vicinity of Zn_{In}^{-} defects. The concentration of Ag in AIS is much lower than that of In, therefore, the QD surface is mostly In-rich leading to a preferential In replacement by Zn^{2+} in agreement with the observed decreased In:Ag ratio (3.0 for the core AIS QDs vs. 2.5 for core/shell AIS/ZnS. As a result, the effect of Zn introduction on the Ag XPS signal is less pronounced. The S 2p signal for the core/shell QDs can be fitted similarly as for the core with two doublets at 161.6 (inorganic sulfide) and 162.6 eV (GSH ligands), while in contrast to the AIS core QDs no sign of oxidized species is detectable. The Ag/S ratio calculated from XPS measurements is 13.5 (vs. 6.7 for AIS core QDs), highlighting the further increased concentration of S with respect to Ag and In after Zn incorporation. This high sulfur content cannot be fully explained by the ZnS shell formation (S/Zn ratio of 5.6) but is attributed to a thicker organic layer as indicated by the DLS data (**Fig. S4**).

Influence of experimental parameters

To optimize the PL properties of the AIS QDs, we investigated the effect of temperature, pressure, and reaction time on the PL intensity. Only one parameter was changed at a time and the precursor ratio of Ag:In:S = 1:4:5, optimized independently, was kept constant. Noteworthy, no clear correlation between any of the experimental parameters studied and the final In:Ag ratio could be established: while in all experiments a feed ratio of 4:1 has been used, the experimental values determined by ICP vary between 2.0 and 4.3 (cf. **Table S2**), in agreement with the XPS results.

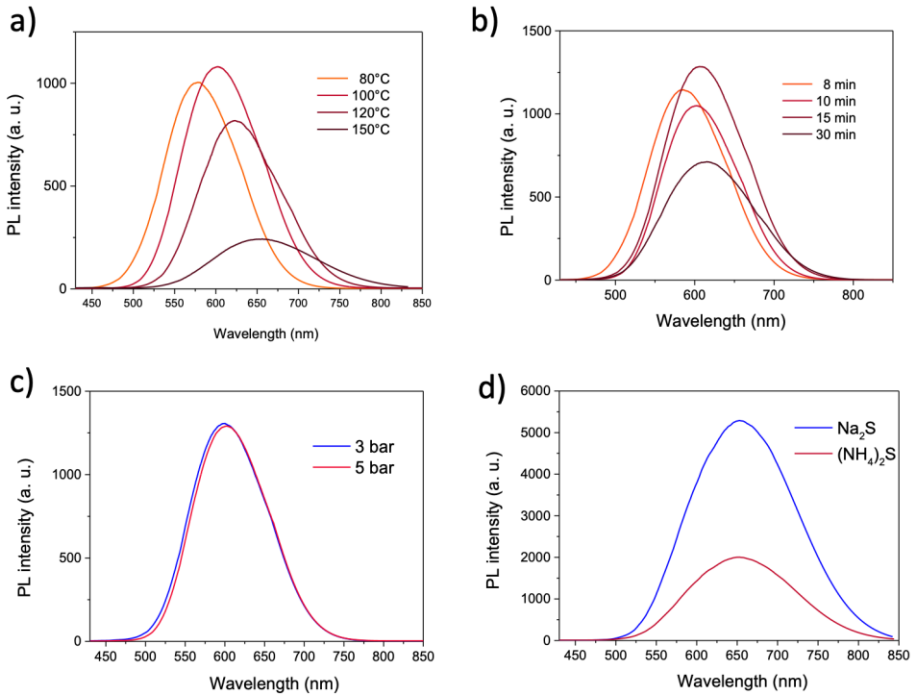

Figure 3: Effect of the temperature (for 8 min reaction time and 3 bar), residence time (at 100°C, 3 bar), pressure, and nature of the sulfur precursors on the PL properties of AIS core nanocrystals (c/d: 8 min, 100°C). The corresponding UV-vis absorption spectra are depicted in **Fig. S8**.

As observed in **Fig. 3a**, the increase of the temperature of the reaction from 80°C to 150°C significantly shifts the maximum wavelength towards the red (from 588 to 668 nm), while the maximum PL intensity is obtained at 100°C. This redshift can be attributed to the size increase of the AIS core NCs as evidenced by DLS measurements: for a reaction time of 8 min (pressure: 3 bar), the hydrodynamic diameter was in the range of 2.3-2.7 nm at 80°C, 3.5-3.6 nm at 100°C, 3.75-3.9 nm at 120°C and 9.5 nm at 150°C. At the same time, the FWHM increases with temperature from 109 nm (391 meV) at 80°C to 158 nm (489 meV) at 150°C. The PLQY is lower at 80°C (<30%), oscillates between 30 and 42% at temperatures in the range of 100°C – 120°C, and drops to 12% at 150°C. Finally, the TRPL data of different samples obtained at 100-120°C and residence times of 8-10 min demonstrated a very similar behavior with average

lifetimes of around 860 ns (cf. **Table S3**, Supp. Inf.). It should be noted that the time economy compared to batch syntheses is significant: while one hour is necessary for the equivalent batch syntheses, the reaction time used in the continuous flow synthesis can be as low as 8 or 10 min without reducing the reaction yield (around 70% for the AIS core QD synthesis) and achieving QDs with equivalent or even better PL properties. As expected, increasing the reaction time leads to larger particle sizes with redshifted emission (cf. **Fig. 3b**), which has been confirmed by DLS measurements: at 100°C and 3 bar a hydrodynamic diameter of 3.56 ±0.5 nm was obtained after 8 min, 3.73±0.9 nm after 10 min, and 4.13±0.8 nm after 15 min, while for longer reaction times (30 min) no further size increase was observed. The pressure (3 or 5 bar) applied in the tubular reactor does not seem to have an impact on the photophysical properties of the QDs (**Fig. 3c**).

As a further parameter of interest, we investigated the use of $(NH_4)_2S$ as the sulfur precursor instead of Na_2S. In addition to its toxicity, Na_2S is a highly hygroscopic compound, which makes it difficult to know precisely its state of hydration and hence the quantity to use in syntheses. In terms of the optical properties, no significant differences are observed for QDs prepared with one or the other precursor (**Fig. 3d**). Additional tests were also carried out with thiourea, which is known to be less reactive than the former two sulfur precursors. However, the formation of gas during the reaction leads to an important pressure increase incompatible with its use in the (closed) continuous flow system. Finally, the excellent reproducibility and scalability of the syntheses have been confirmed by further control experiments (cf. **Fig. S8**).

For the core/shell synthesis also the influence of a number of parameters on the optical properties has been investigated comprising the reaction temperature, the residence time, the amount of shell precursor, the pH of the ZnS solution, and the nature of the core used.

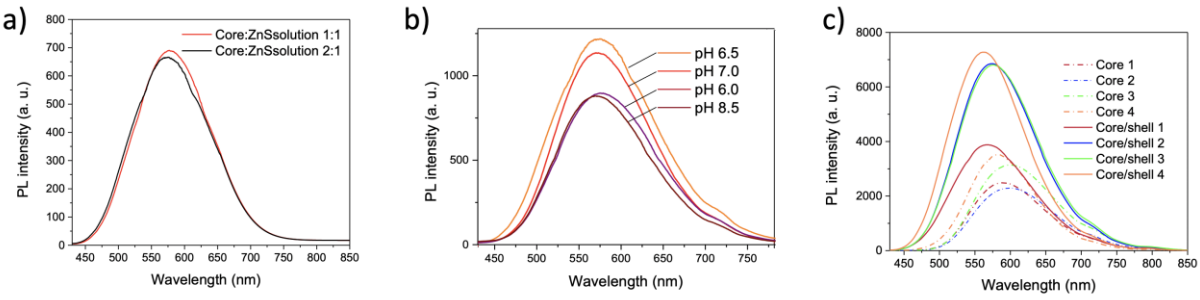

Figure 4: Effect of a) the amount of shell precursor added; b) the pH of the ZnS solution; c) the nature of the AIS core on the PL properties of the obtained AIS/ZnS core/shell QDs (corresponding UV-vis absorption spectra: cf. **Fig. S9**).

As visible in **Fig. 4a**, increasing the amount of the ZnS shell precursor solution by a factor of 2 does not affect the properties. The same applies to a change of the reaction temperature from 100°C to 120°C (not shown). The TRPL data shows an increase by around 250 ns in the average PL lifetime compared to the core, from 863 ns to 1115 ns for both temperatures. This increase is mainly the consequence of the extension of the longest component τ3 (**Table S3 & S4**, Supp. Inf.). As discussed earlier, this component is usually attributed to donor-acceptor pair recombination processes involving core states. Therefore, its modification can be considered as a further manifestation of the partial cation exchange / zinc diffusion into the AIS core during the shell growth, which has already been assumed based on the XRD, XPS, and elemental analysis data (vide supra). Concerning the pH of the ZnS solution, for values around neutral pH (6.5 and 7.0) the maximum PL intensity is observed, while all values lead to a similar blue shift of the emission wavelength to 570-575 nm compared to the core QDs (600-610 nm, cf. **Fig. 4b**). Finally, some influence on the emission properties of the AIS/ZnS core/shell QDs is observed when changing the core AIS QDs (**Fig. 4c**), albeit with no direct correlation between the core and core/shell PL intensity. As for the AIS core synthesis, the time gain compared to

the batch synthesis is significant (15 min instead of 60), and the reproducibility of the shell growth is excellent with the setup used.

Taking together the optical, structural and elemental analysis data of a larger number of samples, the following observations can be made comparing the AIS core to the AIS/ZnS core/shell structure (cf. **Table 2**): i) the average In:Ag ratio goes down from 3.87 to 2.69 due to cation exchange and partial diffusion of Zn into the core (cf. **Table S1**); ii) considering the sizes determined with TEM (core: 1.67 nm, shell: 2.35 nm), which are characteristic for the samples obtained using the optimized conditions, the average composition of the core is $Ag_{0.26}InS_{1.63}$ and that of the core/shell system $Ag_{0.37}InZn_{0.67}S_{2.35}/Zn_{1.63}S_{1.63}$ (assuming charge neutrality for the calculation of the S contents). These values lead to a nominal composition of a single core QD of $Ag_{11}In_{43}S_{70}$ and of a core/shell QD of $Ag_{10}In_{27}Zn_{18}S_{64}/(ZnS)_{110}$. iii) ZnS shell growth induces passivation of surface states and hence a reduction of the contribution of the shortest PL lifetime component $\tau 1$. At the same time, a significant portion of the added zinc ions diffuses into the AIS core, creating additional disorder and Zn_{In} antisite defects, which is the main origin of observed enhancement of the PLQY, the blue-shift of the emission peak, and the increase of the slowest lifetime component $\tau 3$ in the case of the core/shell QDs. We note that the reduction of the number of In atoms in the initial AIS core (16) almost perfectly matches the number of Zn atoms in the ZAIS core (18), in line with the mentioned Zn_{In} antisite defect formation.

Table 2: Average values of PL lifetimes, elemental ratios, size (DLS), and composition of the AIS core and AIS/ZnS core/shell QDs.

	$\tau 1$ (ns) -A_1	$\tau 2$ (ns) -A2	$\tau 3$ (ns) -A3	$\tau_{average}$ (ns)	In:Ag ratio	Zn:In ratio	Size (DLS)	Composition	Composition of 1 QD
AIS core	21.3 - 1.0%	211 - 25.7%	916 - 73.3%	873	3.87	N.A.	3.80 ±0.5 nm	$AgIn_{3.9}S_{6.35}$	$Ag_{11}In_{43}S_{70}$
AIS/ZnS core/shell	23.7 - 0.7%	228 - 26.2%	1178 - 73.1%	1116	2.69	2.30	13.5 ±2.9 nm	$AgIn_{2.7}Zn_{1.8}S_{6.35}$/ $Zn_{4.4}S_{4.4}$	$Ag_{10}In_{27}Zn_{18}S_{64}$/ $(ZnS)_{110}$

Conclusions

We presented the aqueous synthesis of AIS and AIS/ZnS QDs using a flow chemistry approach, which gives access to highly luminescent samples in a very reproducible manner. A number of experimental parameters have been investigated and optimized for maximizing the PLQY, culminating at 83% in this study. The combination of elemental and XPS analyses with steady-state and time-resolved PL spectroscopy indicates that the comparably high PLQY of the AIS core QDs (32% on average) can be attributed to the large density of defect states, such as $[In_{Ag}^{2+} + 2\ V_{Ag}^{-}]$ defect complexes, which are involved in DAP recombination processes. Their formation is favored by the synthetic conditions used, in particular the large In:Ag ratio (around 4:1), the low reaction temperature (100-120°C), and short reaction time, factors expected to induce pronounced structural disorder. The addition of the shell precursors, also achieved using the same continuous flow setup, leads in addition to the ZnS shell formation also to significant diffusion of Zn ions into the AIS core. This process generates novel defect sites, such as Zn_{In}^{-} antisite defects, which are, together with the passivation of non-radiative surface recombination centers, at the origin of the observed PL enhancement to 77% on average, i.e., by a factor of 2.4, of the AIS/ZnS core/shell QDs. The synthetic scheme is very robust, and the proposed continuous flow process can be easily scaled up for producing large quantities of highly luminescent, toxic heavy metal-free AIS/ZnS QDs for various applications encompassing lighting, displays, and (bio-)detection.

Supporting Information.

Description of the flow chemistry setup, Tauc plots, size histograms, DLS data, NMR data, XPS survey spectra, addition PL and UV-vis spectra and property summary tables for samples obtained with different reaction parameters.

Acknowledgments

The authors acknowledge financial support from Région Auvergne-Rhône-Alpes (CPER 2018 AURA P3 MINATEC LABS) and from the French Research Agency ANR (grant ANR 18-CE09-0039-01 FLUO). This work used the platforms of the Grenoble Instruct-ERIC Centre (ISBG; UMS 3518 CNRS-CEA-UGA-EMBL) with support from FRISBI (ANR-10-INSB-05-02) and GRAL (ANR-10-LABX-49-01) within the Grenoble Partnership for Structural Biology (PSB). The IBS electron microscope facility is supported by the Auvergne-Rhône-Alpes Region, the fonds FEDER, the Fondation Recherche Médicale (FRM), and the GIS-IBISA. We thank Hayley Melville (Moltech Anjou, Université d'Angers) for the PESA measurements and Pascal Besesty for his help and fruitful discussions during the initiation period of this project.

References

1. Alivisatos, P., The use of nanocrystals in biological detection. *Nat. Biotechnol.* **2004,** *22* (1), 47-52.

2. Gao, X.; Yang, L.; Petros, J. A.; Marshall, F. F.; Simons, J. W.; Nie, S., In vivo molecular and cellular imaging with quantum dots. *Curr. Opin. Biotechnol.* **2005,** *16* (1), 63-72.

3. Michalet, X.; Pinaud, F. F.; Bentolila, L. A.; Tsay, J. M.; Doose, S.; Li, J. J.; Sundaresan, G.; Wu, A. M.; Gambhir, S. S.; Weiss, S., Quantum Dots for Live Cells, in Vivo Imaging, and Diagnostics. *Science* **2005,** *307* (5709), 538-544.

4. Wegner, K. D.; Hildebrandt, N., Quantum dots: bright and versatile in vitro and in vivo fluorescence imaging biosensors. *Chem. Soc. Rev.* **2015,** *44* (14), 4792-4834.

5. Smith, A. M.; Duan, H.; Mohs, A. M.; Nie, S., Bioconjugated quantum dots for in vivo molecular and cellular imaging. *Advanced Drug Delivery Reviews* **2008,** *60* (11), 1226-1240.

6. Ma, F.; Li, C.-c.; Zhang, C.-y., Development of quantum dot-based biosensors: principles and applications. *Journal of Materials Chemistry B* **2018,** *6* (39), 6173-6190.

7. Probst, C. E.; Zrazhevskiy, P.; Bagalkot, V.; Gao, X., Quantum dots as a platform for nanoparticle drug delivery vehicle design. *Adv Drug Deliv Rev* **2013,** *65* (5), 703-18.

8. Kairdolf, B. A.; Smith, A. M.; Stokes, T. H.; Wang, M. D.; Young, A. N.; Nie, S., Semiconductor Quantum Dots for Bioimaging and Biodiagnostic Applications. *Annual Rev. Anal. Chem.* **2013,** *6* (1), 143-162.

9. Khan, Q.; Subramanian, A.; Ahmed, I.; Khan, M.; Nathan, A.; Wang, G.; Wei, L.; Chen, J.; Zhang, Y.; Bao, Q., Overcoming the Electroluminescence Efficiency Limitations in Quantum-Dot Light-Emitting Diodes. *Advanced Optical Materials* **2019,** *7* (20), 1900695.

10. Weiss, E. A., Designing the Surfaces of Semiconductor Quantum Dots for Colloidal Photocatalysis. *ACS Energy Letters* **2017,** *2* (5), 1005-1013.

11. Hardman, R., A Toxicologic Review of Quantum Dots: Toxicity Depends on Physicochemical and Environmental Factors. *Environ. Health Perspect.* **2006,** *114* (2), 165-172.

12. Zhu, C.; Chen, Z.; Gao, S.; Goh, B. L.; Samsudin, I. B.; Lwe, K. W.; Wu, Y.; Wu, C.; Su, X., Recent advances in non-toxic quantum dots and their biomedical applications. *Progress in Natural Science: Materials International* **2019,** *29* (6), 628-640.

13. Reiss, P.; Carrière, M.; Lincheneau, C.; Vaure, L.; Tamang, S., Synthesis of Semiconductor Nanocrystals, Focusing on Nontoxic and Earth-Abundant Materials. *Chem. Rev.* **2016,** *116* (18), 10731-10819.

14. Aldakov, D.; Reiss, P., Safer-by-Design Fluorescent Nanocrystals: Metal Halide Perovskites vs Semiconductor Quantum Dots. *J. Phys. Chem. C* **2019,** *123* (20), 12527-12541.

15. Aldakov, D.; Lefrancois, A.; Reiss, P., Ternary and quaternary metal chalcogenide nanocrystals: synthesis, properties and applications. *J. Mater. Chem. C* **2013,** *1* (24), 3756-3776.

16. Berends, A. C.; Mangnus, M. J. J.; Xia, C.; Rabouw, F. T.; de Mello Donega, C., Optoelectronic Properties of Ternary I–III–VI2 Semiconductor Nanocrystals: Bright Prospects with Elusive Origins. *J. Phys. Chem. Lett.* **2019,** *10* (7), 1600-1616.

17. Kolny-Olesiak, J.; Weller, H., Synthesis and Application of Colloidal CuInS2 Semiconductor Nanocrystals. *ACS Appl. Mater. Interf.* **2013,** *5* (23), 12221-12237.

18. Coughlan, C.; Ibáñez, M.; Dobrozhan, O.; Singh, A.; Cabot, A.; Ryan, K. M., Compound Copper Chalcogenide Nanocrystals. *Chem. Rev.* **2017,** *117* (9), 5865-6109.

19. Moodelly, D.; Kowalik, P.; Bujak, P.; Pron, A.; Reiss, P., Synthesis, photophysical properties and surface chemistry of chalcopyrite-type semiconductor nanocrystals. *J. Mater. Chem. C* **2019,** *7* (38), 11665-11709.

20. Delices, A.; Moodelly, D.; Hurot, C.; Hou, Y.; Ling, W. L.; Saint-Pierre, C.; Gasparutto, D.; Nogues, G.; Reiss, P.; Kheng, K., Aqueous Synthesis of DNA-Functionalized

Near-Infrared AgInS2/ZnS Core/Shell Quantum Dots. *ACS Appl. Mater. Interf.* **2020,** *12* (39), 44026-44038.

21. Hamanaka, Y.; Ogawa, T.; Tsuzuki, M.; Kuzuya, T., Photoluminescence Properties and Its Origin of AgInS2 Quantum Dots with Chalcopyrite Structure. *J. Phys. Chem. C* **2011,** *115* (5), 1786-1792.

22. Bai, X.; Purcell-Milton, F.; Gun'ko, Y. K., Optical Properties, Synthesis, and Potential Applications of Cu-Based Ternary or Quaternary Anisotropic Quantum Dots, Polytypic Nanocrystals, and Core/Shell Heterostructures. *Nanomaterials* **2019,** *9* (1), 85.

23. Yarema, O.; Yarema, M.; Wood, V., Tuning the Composition of Multicomponent Semiconductor Nanocrystals: The Case of I–III–VI Materials. *Chem. Mater.* **2018,** *30* (5), 1446-1461.

24. Jing, L.; Kershaw, S. V.; Li, Y.; Huang, X.; Li, Y.; Rogach, A. L.; Gao, M., Aqueous Based Semiconductor Nanocrystals. *Chem. Rev.* **2016,** *116* (18), 10623-10730.

25. Raevskaya, A.; Lesnyak, V.; Haubold, D.; Dzhagan, V.; Stroyuk, O.; Gaponik, N.; Zahn, D. R. T.; Eychmüller, A., A Fine Size Selection of Brightly Luminescent Water-Soluble Ag–In–S and Ag–In–S/ZnS Quantum Dots. *J. Phys. Chem. C* **2017,** *121* (16), 9032-9042.

26. Stroyuk, O.; Raevskaya, A.; Spranger, F.; Selyshchev, O.; Dzhagan, V.; Schulze, S.; Zahn, D. R. T.; Eychmüller, A., Origin and Dynamics of Highly Efficient Broadband Photoluminescence of Aqueous Glutathione-Capped Size-Selected Ag–In–S Quantum Dots. *J. Phys. Chem. C* **2018,** *122* (25), 13648-13658.

27. Martynenko, I. V.; Baimuratov, A. S.; Weigert, F.; Soares, J. X.; Dhamo, L.; Nickl, P.; Doerfel, I.; Pauli, J.; Rukhlenko, I. D.; Baranov, A. V.; Resch-Genger, U., Photoluminescence of Ag-In-S/ZnS quantum dots: Excitation energy dependence and low-energy electronic structure. *Nano Research* **2019,** *12* (7), 1595-1603.

28. Mirhosseini Moghaddam, M.; Baghbanzadeh, M.; Sadeghpour, A.; Glatter, O.; Kappe, C. O., Continuous-Flow Synthesis of CdSe Quantum Dots: A Size-Tunable and Scalable Approach. *Chemistry – A European Journal* **2013,** *19* (35), 11629-11636.

29. Akdas, T.; Haderlein, M.; Walter, J.; Apeleo Zubiri, B.; Spiecker, E.; Peukert, W., Continuous synthesis of CuInS2 quantum dots. *RSC Advances* **2017,** *7* (17), 10057-10063.

30. Nette, J.; Howes, P. D.; deMello, A. J., Microfluidic Synthesis of Luminescent and Plasmonic Nanoparticles: Fast, Efficient, and Data-Rich. *Advanced Materials Technologies* **2020,** *5* (7), 2000060.

31. Li, S.; Chen, Y.; Huang, L.; Pan, D., Simple continuous-flow synthesis of Cu–In–Zn–S/ZnS and Ag–In–Zn–S/ZnS core/shell quantum dots. *Nanotechnology* **2013,** *24* (39), 395705.

32. Ma, H.; Pan, L.; Wang, J.; Zhang, L.; Zhang, Z., Synthesis of AgInS2 QDs in droplet microreactors: Online fluorescence regulating through temperature control. *Chin. Chem. Lett.* **2019,** *30* (1), 79-82.

33. Soares, J. X.; Wegner, K. D.; Ribeiro, D. S. M.; Melo, A.; Häusler, I.; Santos, J. L. M.; Resch-Genger, U., Rationally designed synthesis of bright AgInS2/ZnS quantum dots with emission control. *Nano Research* **2020,** *13* (9), 2438-2450.

34. Delices, A.; Moodelly, D.; Hurot, C.; Hou, Y.; Ling, W. L.; Saint-Pierre, C.; Gasparutto, D.; Nogues, G.; Reiss, P.; Kheng, K., Aqueous Synthesis of DNA-Functionalized Near-Infrared AgInS ₂ /ZnS Core/Shell Quantum Dots. *ACS Appl. Mater. Interf.* **2020,** *12* (39), 44026-44038.

35. Parani, S.; Oluwafemi, O. S., Selective and sensitive fluorescent nanoprobe based on AgInS ₂ -ZnS quantum dots for the rapid detection of Cr (III) ions in the midst of interfering ions. *Nanotechnology* **2020,** *31* (39), 395501.

36. Reiss, P.; Protière, M.; Li, L., Core/Shell Semiconductor Nanocrystals. *Small* **2009,** *5* (2), 154-168.

37. Chevallier, T.; Le Blevennec, G.; Chandezon, F., Photoluminescence properties of AgInS2–ZnS nanocrystals: the critical role of the surface. *Nanoscale* **2016,** *8* (14), 7612-7620.

38. Kameyama, T.; Takahashi, T.; Machida, T.; Kamiya, Y.; Yamamoto, T.; Kuwabata, S.; Torimoto, T., Controlling the Electronic Energy Structure of ZnS–AgInS2 Solid Solution Nanocrystals for Photoluminescence and Photocatalytic Hydrogen Evolution. *J. Phys. Chem. C* **2015,** *119* (44), 24740-24749.

39. Cichy, B.; Olejniczak, A.; Bezkrovnyi, O.; Kepinski, L.; Strek, W., Defects mediated charge disturbance in quantum-confined AgxS/AgInS2 random alloys – Toward slowly decaying quantum dot emitters. *J. Alloys Compd.* **2019,** *798*, 290-299.

40. Cichy, B.; Wawrzynczyk, D.; Samoc, M.; Stręk, W., Electronic properties and third-order optical nonlinearities in tetragonal chalcopyrite AgInS2, AgInS2/ZnS and cubic spinel AgIn5S8, AgIn5S8/ZnS quantum dots. *J. Mater. Chem. C* **2017,** *5* (1), 149-158.

41. Mao, B.; Chuang, C.-H.; Wang, J.; Burda, C., Synthesis and Photophysical Properties of Ternary I–III–VI AgInS2 Nanocrystals: Intrinsic versus Surface States. *J. Phys. Chem. C* **2011,** *115* (18), 8945-8954.

42. Dai, M.; Ogawa, S.; Kameyama, T.; Okazaki, K.-i.; Kudo, A.; Kuwabata, S.; Tsuboi, Y.; Torimoto, T., Tunable photoluminescence from the visible to near-infrared wavelength region of non-stoichiometric AgInS2 nanoparticles. *J. Mater. Chem.* **2012,** *22* (25), 12851-12858.

43. Yang, J.; Xia, N.; Wang, X.; Liu, X.; Xu, A.; Wu, Z.; Luo, Z., One-pot one-cluster synthesis of fluorescent and bio-compatible Ag14 nanoclusters for cancer cell imaging. *Nanoscale* **2015,** *7* (44), 18464-18470.

44. Amin, E. A.; Truhlar, D. G., Zn Coordination Chemistry: Development of Benchmark Suites for Geometries, Dipole Moments, and Bond Dissociation Energies and Their Use To Test and Validate Density Functionals and Molecular Orbital Theory. *J Chem Theory Comput* **2008,** *4* (1), 75-85.

45. Minenkov, Y.; Chermak, E.; Cavallo, L., Accuracy of DLPNO–CCSD(T) Method for Noncovalent Bond Dissociation Enthalpies from Coinage Metal Cation Complexes. *Journal of Chemical Theory and Computation* **2015,** *11* (10), 4664-4676.

46. Mrad, M.; Ben Chaabane, T.; Rinnert, H.; Lavinia, B.; Jasniewski, J.; Medjahdi, G.; Schneider, R., Aqueous Synthesis for Highly Emissive 3-Mercaptopropionic Acid-Capped AIZS Quantum Dots. *Inorg. Chem.* **2020,** *59* (9), 6220-6231.

47. Maeda, T.; Takeichi, T.; Wada, T. In *Defect Formation Energies in Chalcopyrite-Type AgInSe2 and the Rerated Chalcopyrite Compounds by First Principles Calculations*, 2006 IEEE 4th World Conference on Photovoltaic Energy Conference, IEEE;: 2006; pp 445-448.

48. Naumkin, A. V.; Kraut-Vass, A.; Gaarenstroom, S. W.; Powell, C. J. NIST Standard Reference Database 20. (accessed 15.07.2022).

49. Chevallier, T.; Benayad, A.; Le Blevennec, G.; Chandezon, F., Method to determine radiative and non-radiative defects applied to AgInS2–ZnS luminescent nanocrystals. *Physical Chemistry Chemical Physics* **2017,** *19* (3), 2359-2363.

50. Lee, A. Y.; Blakeslee, D. M.; Powell, C. J.; Rumble, J., J.R., Development of the web-based NIST X-ray Photoelectron Spectroscopy (XPS) Database. *Data Science Journal* **2006,** *1* (1), 1-12.

TOC graphics: